Importance of solar subsurface heating in ocean general circulation models

4 authors, including:

Peter Rochford
Symplectic, LLC

31 PUBLICATIONS **1,392** CITATIONS

SEE PROFILE

Robert Arnone
University of Southern Mississippi

268 PUBLICATIONS **4,551** CITATIONS

SEE PROFILE

Some of the authors of this publication are also working on these related projects:

Maritime Advanced Geospatial Intelligence Craft View project

VIIRS val/cal View project

Importance of solar subsurface heating in ocean general circulation models

Peter A. Rochford

Naval Research Laboratory, Stennis Space Center, Mississippi, USA

A. Birol Kara[1]

Sverdrup Technology Inc , Stennis Space Center, Mississippi, USA

Alan J. Wallcraft and Robert A. Arnone

Naval Research Laboratory, Stennis Space Center, Mississippi, USA

Abstract. The importance of subsurface heating on surface mixed layer properties in an ocean general circulation model (OGCM) is examined using attenuation of solar irradiance with depth below the ocean surface. The depth-dependent attenuation of subsurface heating is given by global monthly mean fields for the attenuation of photosynthetically available radiation (PAR), k_{PAR}. These global fields of k_{PAR} are derived from Sea-viewing Wide Field-of-view Sensor (SeaWiFS) data on the spectral diffuse attenuation coefficient at 490 nm (k_{490}), and have been processed to have the smoothly varying and continuous coverage necessary for use in OGCM applications. These monthly fields provide the first complete global data sets of subsurface optical fields that can be used for OGCM applications of subsurface heating and bio-optical processes. The effect on global OGCM prediction of sea surface temperature (SST) and surface mixed layer depth (MLD) is examined when solar heating, as given by monthly mean k_{PAR} and PAR fields, is included in the model. It is found that subsurface heating yields a marked increase in the SST predictive skill of the OGCM at low latitudes. No significant improvement in MLD predictive skill is obtained when including subsurface heating. Use of the monthly mean k_{PAR} produces an SST decrease of up to 0.8°C and a MLD increase of up to only 4–5 m for climatological surface forcing, with this primarily confined to the equatorial regions. Remarkably, a constant k_{PAR} value of 0.06 m^{-1} , which is indicative of optically clear open ocean conditions, is found to serve very well for OGCM prediction of SST and MLD over most of the global ocean.

1. Introduction

The solar heating of the upper ocean occurs through the absorption of solar irradiance (400–800 nm) with depth beneath the ocean surface, with this rate of absorption varying in space and time. The distribution of this solar heating with depth within the surface mixed layer directly affects the sea surface temperature (SST) [e.g., *Kantha and Clayson*, 1994]. It also indirectly affects the mixed layer depth (MLD) by altering the vertical turbulent mixing in the upper water column [e.g., *Lewis et al.*, 1990]. The positive buoyancy forcing generated by this subsurface heating is primarily responsible for stabilizing the surface waters [e.g., *Martin*, 1985], which in turn contributes to the formation of the upper ocean thermocline.

Knowledge of the seasonal and maximum annual depth of the thermocline is of importance for heat storage in the ocean [*White et al.*, 1998; *Gallimore and Houghton*, 1987; *Meehl*, 1984; *Stevenson and Niiler*, 1983]. SST prediction in one-dimensional mixed layer models has been shown to be sensitive to the parameterization of the solar extinction with depth in the upper water column when there is a shallow mixed layer [*Kantha and Clayson*, 1994; *Martin*,

1985]. This is because the solar radiation can penetrate to depths below the surface mixed layer under such circumstances, thereby requiring that proper account be taken of the solar heating within the mixed layer.

Studies have indicated the necessity of including penetrating solar irradiance for SST predictions in the tropical Pacific [*Zaneveld et al.*, 1981; *Woods et al.*, 1984, *Lewis et al.*, 1990]. While this has been clearly shown with one-dimensional models, the majority of ocean general circulation models (OGCM) with mixed layers do not consider space- and time-varying solar attenuation with depth [*Baturin and Niiler*, 1997; *Carton and Zhou*, 1997; *Murtugudde et al.*, 1995; *Schopf and Loughe*, 1995; *Sterl and Kattenberg*, 1994; *Yuen et al.*, 1992]. The reason is there has been insufficient information on the regional and seasonal distribution of the irradiance absorption coefficient over basin scales to use it as part of the heat flux forcing in an OGCM. As a consequence, the extent to which subsurface heating is important for global SST prediction has been difficult to determine.

Recently available ocean color remote sensing data (1997–1998) being acquired with the Sea-viewing Wide Field-of-view Sensor (SeaWiFS) can now be used to estimate surface attenuation rates on global scales. These data collected from the commencement of SeaWiFS operation in September 1997 provide, for the first time, the global spatial variation of the rate of absorption which can be used to quantify the solar influence in OGCM applications. SeaWiFS ocean color data provide information on water leaving radiances at selected wavelengths [*McClain et al.*, 1998], from which the wavelength dependence of the diffuse attenuation coefficient can be constructed for the photosyntheti-

[1]Now at Center for Ocean-Atmospheric Prediction Studies, Florida State University, Tallahassee, Florida, USA.

cally available radiation (PAR) portion of the solar spectrum. PAR is defined as the portion of the spectrum that penetrates beyond a few centimeters of the surface and represents the light available for photosynthesis [e.g., *Mobley*, 1994]. The diffuse attenuation coefficient at 490 nm (k_{490}) is in particular abundance because the strong pigment absorption at 490 nm in phytoplankton is of interest in remote sensing [*Gordon and Clark*, 1980]. Given that 490 nm lies within the 420–580 nm wavelength range having the deepest penetration into the ocean [*Austin and Petzold*, 1986; *Morel*, 1988], knowledge of k_{490} allows the attenuation of PAR (k_{PAR}) to be easily determined [*Austin and Petzold*, 1986]. In the past, such remote sensing data, which were available from sensors, such as the Coastal Zone Color Scanner [e.g., *Arnone et al.*, 1992], were too limited in areal coverage to be used as part of the heat flux forcing in a basin-scale OGCM. However, with SeaWiFS now in operation since September 1997, sufficient ocean color data at high-resolution global coverage have been acquired to construct a complete annual cycle of monthly means that can be used for OGCM forcing.

In addition to SST, knowledge of the attenuation of PAR with depth, as given by the k_{PAR} monthly fields, can be used to characterize the light environment for models of ocean biology [*Dadou et al.*, 1996; *Flierl and Davis*, 1993; *Keen et al.*, 1997; *McCreary et al.*, 1996]. The variation of solar irradiance with depth defines the euphotic zone of the upper ocean, where photosynthesis can occur, and has a direct influence upon growth rates for phytoplankton. The vertical PAR distribution directly controls the rate of photosynthesis within the phytoplankton subcommunity of the ocean ecosystem [e.g., *Platt et al.*, 1988]. As phytoplankton are an important first link in the food chain, the variation of PAR with depth has a strong and direct impact on primary production and therefore the world's fisheries. The availability of these k_{PAR} fields provides the opportunity to implement satellite-based optics in biophysical coupled OGCMs of primary productivity [*Keen et al.*, 1997; *McCreary et al.*, 1996].

In this study we report for the first time on the construction of k_{490} and k_{PAR} data sets of monthly means from recently available 1997–1998 SeaWiFS ocean color data and comment on the consequences of its general variability for subsurface heating (section 2). We then use this satellite-derived data set as part of the heat flux forcing in the global Naval Research Laboratory (NRL) Layered Ocean Model (NLOM) with an embedded mixed layer (section 3) and report on its consequences for SST and mixed layer depth (MLD) prediction (section 4) when using climatological surface forcing. Finally, a conclusion is rendered (section 5) on the relative importance of including subsurface heating effects in an OGCM for prediction of surface mixed layer properties.

2. Optical Attenuation With Ocean Depth

2.1. Background

The solar irradiance at the ocean surface ranges in wavelength from ~300 to 2800 nm and is composed of three general regions: the ultraviolet (UV) below 400 nm, the visible 400–700 nm, and the infrared (IR) above 700 nm. Approximately half of the solar irradiance occurs in the infrared, and most of this is absorbed and converted to heat within the first few centimeters of the upper ocean [*Mobley*, 1994]. The remaining incident solar irradiance that penetrates below the ocean surface is predominantly in the visible and UV, and this is regulated through optical absorption by the water, phytoplankton, and suspended particles [*Mobley*, 1994]. This latter portion of the spectrum is referred to as PAR because of its importance for biological processes. PAR is defined as the 350–700 nm range of the spectrum and accounts for 43–50% of the solar irradiance at the sea surface [*Mobley*, 1994]. It comprises most of the solar irradiance that penetrates to depths >1 m and is

the quantity of interest for subsurface solar heating in an OGCM with an embedded mixed layer.

The attenuation of surface solar irradiance (Q_{SOL}) with depth z over the solar spectrum is typically represented as a simple exponential decay,

$$Q_{SOL}(\lambda, z) = Q_{SOL}(\lambda, 0) \exp(-k_\lambda z), \quad (1)$$

where k_λ is defined as the spectral diffuse attenuation coefficient at wavelength λ. The k_λ values vary strongly as a function of the optical characteristics of the water, such as the amount of suspended particles. There are methods for specifying k_λ given the known attenuation at a single wavelength λ_0 [*Austin and Petzold*, 1986; *Morel*, 1988] or via sets of parameters for different Jerlov water types [*Zaneveld and Spinrad*, 1980]. Typically, subsurface heating is calculated by dividing the solar spectrum into a number of narrow wavelength bands [e.g., *Paulson and Simpson*, 1977; *Morel and Antoine*, 1994], with k_λ calculated at the center wavelength for each of the bands. However, it is also possible to derive a simple exponential decay for the attenuation of PAR with depth, which is given in terms of a single wavelength λ_0 [*Austin and Petzold*, 1986]. This allows a simpler expression to be used

$$PAR(z) = PAR(0) \exp(-k_{PAR} z), \quad (2)$$

where PAR(0) is the PAR at the ocean surface. For OGCM with bulk mixed layers, where the upper ocean is typically represented by a vertically uniform layer <5–10 m, this provides a sufficiently accurate attenuation of PAR for modeling purposes. For the majority of OGCM that include a nonbulk mixed layer parameterization [e.g., *Kantha and Clayson*, 1994; *Large et al.*, 1994], this k_{PAR} parameterization may also be appropriate, as many such OGCM use a relatively coarse vertical resolution to represent the upper ocean.

For this study we elect to use an attenuation coefficient for PAR (k_{PAR}) that has a dependence upon a reference wavelength λ_0. Such a relationship has been determined through a set of regressions on data obtained in the North Pacific Ocean [*Zaneveld et al.*, 1993]. This relationship uses $\lambda_0 = 488$ nm,

$$k_{PAR} = \begin{cases} 0.0085 + 1.6243 k_{488} & k_{488} \leq 1 \\ 0.3175 + 1.2144 k_{488} & 1 < k_{488} \leq 2.3 \\ 0.3570 + 1.1676 k_{488} & 2.3 < k_{488}, \end{cases} \quad (3)$$

and varies according to three different water classes: oligotrophic clear CASE 1 waters, intermediate CASE 1–2 waters, and turbid coastal CASE 2 waters. Note these relations are not continuous at $k_{488} = 1$ and 2.3 because they have been obtained from independent regressions over the k_{488} intervals [0, 1], [1, 2.3], and [2.3, 4.6]. We have removed the upper limit for the turbid coastal CASE 2 waters as there are few regions having optical attenuation greater than $k_{488} = 4.6$.

Empirical relationships also have been derived between the ratio of two spectral channels (490 nm/550 nm) and the surface attenuation coefficient [*Austin and Petzold*, 1986; *O'Reilly et al.*, 2000]. These relationships have been shown to be robust (in CASE 1 and 2 waters) if accurate water leaving radiances can be derived from SeaWiFS. Improved atmospheric correction methods with SeaWiFS have provided improved estimates of k_{490} [*McClain et al.*, 2000a, 2000b; *O'Reilly et al.*, 2000]. Since remotely sensed measurements of optical attenuation in seawater is typically obtained at 490 nm we shall henceforth use (3) with k_{488} substituted by k_{490}. This introduces negligible error into the estimate of k_{PAR}.

2.2. Methodology

At the time this study was initiated, the SeaWiFS project only provided k_{490} data collected from 1 October 1997 through to 30

September 1998 [*McClain et al.*, 1998]. These data have been averaged and binned by the SeaWiFS Project at NASA Goddard Space Flight Center (NASA GSFC) into daily, weekly, monthly, and annual means and have been made available as part of their Level-3 binned data products [*Darzi*, 1998]. We acquired the monthly mean k_{490} data, which are simple averages of the inferred k_{490}, from the available scenes of the 1997–1998 observation period. The details on the algorithms used to infer and bin the k_{490} from the sensor observations are available in SeaWiFS technical reports [e.g., *Firestone and Hooker*, 1998] and will not be given here. These data products have a resolution of 9 km (~1/12°) but with an incomplete spatial and temporal coverage. We choose to process this data using the SeaWiFS Data Analysis System (SeaDAS) [*Fu et al.*, 1998] to produce globally gridded fields at 1° resolution spanning from 0.5°E, 89.5°S to 359.5°E, 89.5°N. This 360 × 180 grid configuration is chosen to be consistent with climatologies in general use within the scientific community [*Da Silva et al.*, 1994; *Levitus and Boyer*, 1994; *Levitus et al.*, 1994].

As with all remotely sensed data, the SeaWiFS k_{490} suffers from problems of data voids because of cloud coverage and/or infrequent sampling by satellite sensors as well as incorrect and biased observations (noise) because of sensor limitations. The SeaWiFS algorithm used here comes from the initial processing of the distributed data archive and does not have the corrections that are applied for turbid water regions in the reprocessed data (see section 2.3). Even with the large number of scenes used to construct the monthly k_{490} data sets, they contain ocean regions of sparse data. The most prominent region is around the Antarctic Ocean in the vicinity of the Weddell Sea. To fill in these data voids in the monthly k_{490}, we begin by interpolating over time using a one-dimensional periodic cubic spline with a tension factor of $\sigma = 5.0$ for each location having a data void during the year. To exclude the incorrect values that can arise because of spurious oscillations in the cubic splines, we reject interpolated values that fall outside a range of values uniquely determined for each data void location. A suitable range is found to be 25% of the minimum value to 125% of the maximum value of those monthly mean k_{490} values used to construct the spline coefficients. Data voids in a given month are left unaltered as a first step if the interpolated value is rejected.

After temporal filling, the remaining data voids are replaced by next applying a statistical interpolation (SI) in space for each individual monthly mean, with an exponential correlation function assumed for the covariance (see Appendix A). This approach successfully yields monthly k_{490} means of complete coverage. However, as we noticed, the data sets still suffer from noise problems inherited from the satellite observations. To remove the noise, a three-step process is applied to the k_{490} data. First, the data are checked again for anomalously large or small values. Using the same interpolating grid boxes as in the SI, the mean and standard deviation are calculated for all data values except the one at the box center. The data value at the central location is considered anomalous if it falls outside of the one standard deviation interval for this distribution. Its replacement value is determined by applying SI again. The latest data values are used when making these replacements and can include SI values inserted from earlier in the search. Second, the condition $k_{490} \geq 10^{-5}$ m^{-1} is imposed on all the data values to avoid an infinite $1/k_{490}$ depth scale, should there be such a future need in an OGCM application. The minimum limit of $k_{490} = 10^{-5}$ m^{-1} is chosen so $1/k_{490}$ is comparable to the maximum ocean depth. Third, to remove the remaining minor residual noise, a 3 × 3 spatial filter with a 1:2:1 weighting ($F = 1.0, 2.0, 1.0, 2.0, 4.0, 2.0, 1.0, 2.0, 1.0$) is then passed once over the data to smooth it to a level suitable for OGCM applications.

Using these monthly k_{490} data sets, we construct the global monthly k_{PAR} using the *Zaneveld et al.* [1993] relations as given

in (3). No data filling or noise removal are applied to the k_{PAR} as these problems have been removed from the k_{490} data. We use these k_{PAR} monthly means for prescribing the subsurface heating in our OGCM with a bulk mixed layer as described in further detail in section 3.2. For other OGCM with nonbulk mixed layers the k_{490} data sets may also be used to easily construct k_λ over the full spectrum, and the latter can then used to prescribe the subsurface heating.

2.3. Variability of k_{PAR}

To show the general variability of the optical attenuation over the annual cycle, we present in Plates 1 and 2 the k_{PAR} fields obtained for the middle months of the four seasons. As expected, most of the global open ocean contains regions of relatively clear water ($k_{PAR} = 0.06$ m^{-1}) with k_{PAR}^{-1} optical depths >14 m. Regions of much more opaque waters are the Arabian Sea, North Atlantic and North Pacific Oceans, the western coastal regions of Africa, and some parts of the equatorial ocean and Antarctic, where absorption is greater because of the dominance of phytoplankton. As previously mentioned, there is a strong seasonal variability in optical attenuation over a large part of the Arabian Sea, with the large k_{PAR} values during winter and summer (Figure 1) occurring in conjunction with the northeast and southwest monsoon winds, respectively. These monsoon winds are known to play a major role in the phytoplankton population blooms of this region because they are responsible for upwelling water rich in nutrients [*Brock et al.*, 1991; *Gallacher and Rochford*, 1995].

We note that the Arabian Sea and the western coastal regions of Africa lie adjacent to large desert land areas and are subject to high concentrations of wind borne dust. Atmospheric dust contaminates estimates of k_{490} toward larger values in the SeaWiFS algorithms used in the initial processing of the data. The optical attenuation in these areas may therefore be lower than the k_{PAR} values given in this data set.

In June 2000 the SeaWiFS project completed reprocessing of the data with algorithms having improved atmospheric corrections. A near-infrared correction is applied for turbid water regions in their Level-1 data products, and contaminated pixels are now removed from the Level-3 data products by invoking an absorbing aerosol flag. These provide better estimates of k_{490} that allow us to check for a bias in our k_{PAR} data set used for this study. We created a k_{PAR} monthly climatology using the SeaWiFS reprocessed Level-3 k_{490} data from September 1997 through February 2001. For the Arabian Sea and the western coastal regions of Africa the absolute differences in k_{PAR} between the 1997–1998 and 1997–2000 data sets are ≤0.05 m^{-1}. The largest absolute differences occur in other offshore coastal regions (≤0.5 m^{-1}) and are attributed to the corrections used in the SeaWiFS reprocessing. For open ocean waters we find little change in the k_{PAR} product as the differences are ≤0.02 m^{-1}. These latter differences represent a change of ~1% in PAR(z) at the base of the mixed layer and will not alter the major conclusions of the paper.

To help in the interpretation of the k_{PAR} fields, we establish here a simple association between the Jerlov water types and k_{PAR} values. For each of the Jerlov water classes (I, IA, IB, and II) we approximate the absorption of solar radiation with depth as established by *Jerlov* [1976] with a single exponential decay formula. We fit the data using the formula

$$I(z) = 100(1 - a \exp [-z/(62.0a - b)]), \qquad (4)$$

where $I(z)$ is the percentage absorption of surface irradiance, z is the depth, and a is the Jerlov fraction of solar irradiance penetration at 2 m depth. The parameter b is chosen to reproduce
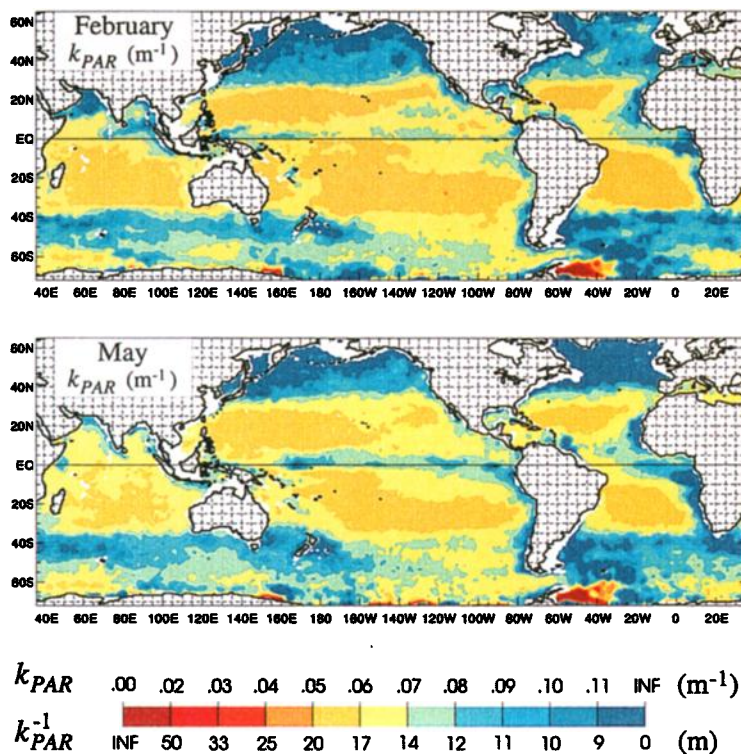
Plate 1. Global attenuation of PAR (k_{PAR}) for the middle month of the Northern Hemisphere winter (February) and spring (May). The global coverage is from 72°S to 65°N of the NLOM domain. The corresponding depth of optical penetration (k_{PAR}^{-1}) is shown on the color bar. Note that $k_{PAR} = 0.06$ m^{-1} represents optically clear water as explained in the text.
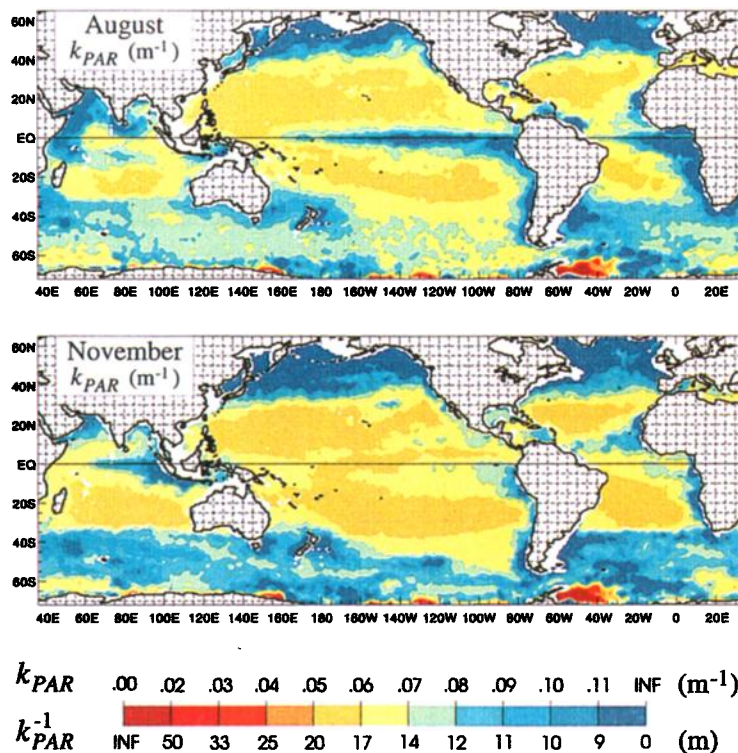

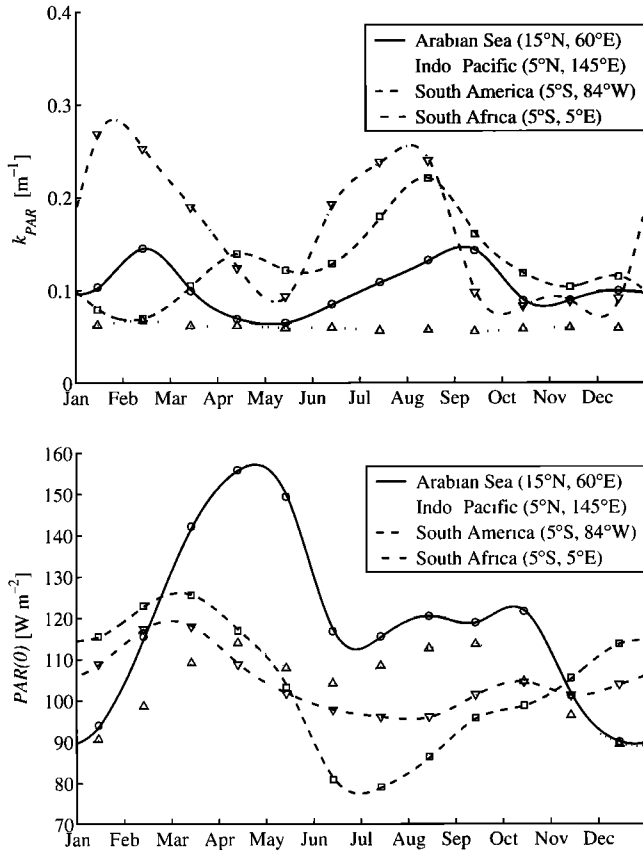**Plate 2.** The same as Figure 1 but for the middle month of the Northern Hemisphere summer (August) and fall (November).

Figure 1. Time series of monthly mean k_{PAR} and PAR at four selected sites in the global ocean where there is large seasonal variability in optical attenuation. A cubic spline interpolation was performed through the monthly mean values of k_{PAR} and PAR indicated by the geometric symbols on the lines. The locations of the time series are indicated by the corresponding symbols in the top panel of Plate 3.

the Jerlov absorption profile best at depths below 10 m because of our present interests for OGCM applications. For this simple approximation one obtains $k_{490} = (62.0a - b)^{-1}$, and from this one obtains k_{PAR} using (3). The parameters for each Jerlov water class along with the k_{PAR} and k_{490} values are given in Table 1. These parameter choices reproduce the Jerlov absorption profiles quite well below 20 m for each of the four water classes (Figure 2). From Table 1 we confirm that k_{PAR} = 0.05 m^{-1} is representative of open ocean conditions (class I), k_{PAR} = 0.06 m^{-1} is representative of optically clear open ocean conditions (class IA), and 0.08 m^{-1} ≤ k_{PAR} ≤ 0.12 m^{-1} indicates quite turbid water (class IB and II).

3. OGCM and Subsurface Solar Heating

3.1. OGCM

The OGCM used for this study is the finite depth version of NLOM with an embedded mixed layer. It is a successor of the reduced-gravity NLOM developed by *Rochford et al.* [2000] for the Indian Ocean, with extensive improvements to address the greater issues associated with implementation on a global basin scale. We limit ourselves here to a short description of the model as a complete presentation is beyond the scope of this study. The version used here will be fully presented in a future paper.

The NLOM uses a primitive equation layered formulation where the equations have been vertically integrated through each Lagrangian layer $k = 1, ..., n$. Prognostic variables are layer density ρ_k, layer thickness h_k, and layer volume transport $\mathbf{V}_k$ (layer velocity $\mathbf{v}_k$ times layer thickness h_k). The bottom topography is confined to the lowest layer, and a finite layer thickness is maintained by mixing across layer interfaces. Following the notation of *Metzger and Hurlburt* [1996, 2001], the governing equations for the prognostic variables are

$$\frac{\partial \mathbf{V}_k}{\partial t} + (\nabla \cdot \mathbf{V}_k + \mathbf{V}_k \cdot \nabla)\mathbf{v}_k + \widehat{k} \times f\mathbf{V}_k$$
$$= \max(0, -\omega_{k-1})\mathbf{v}_{k-1} + \max(0, \omega_k)\mathbf{v}_{k+1}$$
$$- [\max(0, -\omega_k) + \max(0, \omega_{k-1})]\mathbf{v}_k$$
$$+ \max(0, -C_M\omega_{k-1})(\mathbf{v}_{k-1} - \mathbf{v}_k)$$
$$+ \max(0, C_M\omega_k)(\mathbf{v}_{k+1} - \mathbf{v}_k)$$
$$- h_k \left\{ \sum_{l=1}^{n} [G_{kl}\nabla(h_l - H_l) + h_l\nabla G_{kl}] \right.$$
$$\left. - \frac{g}{\rho_o} \left(\sum_{l=1}^{k-1} h_l + \frac{h_k}{2} \right) \nabla\rho_k \right\}$$
$$+ (\tau_{k-1} - \tau_k)/\rho_o + A_H\nabla^2\mathbf{V}_k, \tag{5}$$

$$\frac{\partial h_k}{\partial t} + \nabla \cdot \mathbf{V}_k = \omega_k - \omega_{k-1}, \tag{6}$$

$$\frac{\partial \rho_k}{\partial t} + \mathbf{v}_k \cdot \nabla\rho_k = \frac{\max(0, \omega_k)}{h_k}\Delta\rho_k - \frac{\max(0, -\omega_{k-1})}{h_k}\Delta\rho_{k-1}$$
$$+ \frac{\sigma_\rho H_o}{\min(h_k, 6H_o)}(\widehat{\rho}_k - \rho_k) - \delta_{1k}\frac{\alpha(T_m)(Q_{NET} - \widehat{Q}_{NET})}{C_{pw}h_1}$$
$$+ \frac{K_H}{h_k}\nabla \cdot (h_k\nabla\rho_k). \tag{7}$$

The surface turbulent boundary layer that is embedded within the NLOM is assumed to be "well mixed." The temperature T_m is therefore defined to be constant throughout a layer of thickness h_m and to be equivalent to the SST. The layer thickness h_m is defined as the lower bound of the turbulent boundary layer and is hence the MLD. The embedded mixed layer carries prognostic equations for SST and MLD as follows:

$$\frac{\partial T_m}{\partial t} + \mathbf{v}_1 \cdot \nabla T_m = -\frac{\max(0, \omega_m)}{h_m}(T_m - \Delta T_m - T_b)$$
$$+ \frac{Q_{abs}(h_m)}{\rho_o C_{pa}h_m} + \frac{K_H}{h_m}\nabla \cdot (h_m\nabla T_m) \tag{8}$$

$$\frac{\partial h_m}{\partial t} + \nabla \cdot (h_m \mathbf{v}_1) = \omega_m, \tag{9}$$

where the depth-averaged velocity of water within the mixed layer is assumed to be the same as layer 1. It is the presence of these two prognostic variables that enables subsurface heating effects to be examined with this OGCM, as the SST is directly influenced by solar heating and the MLD is indirectly influenced through buoyancy production from solar heating.

Table 1. Optical Attenuation Values for Jerlov Water Types

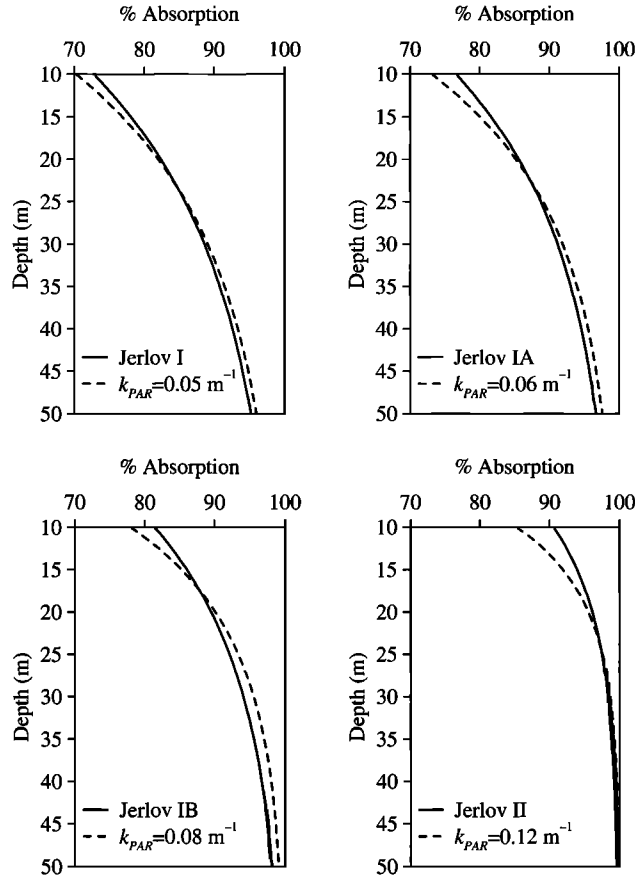| Water Type	a	b	k_{PAR}, m^{-1}	k_{490}, m^{-1}
Jerlov I	0.42	3.0	0.052	0.027
Jerlov IA	0.38	3.0	0.061	0.032
Jerlov IB	0.33	3.0	0.080	0.044
Jerlov II	0.23	3.0	0.124	0.071

Figure 2. Attenuation coefficient k_{PAR} values corresponding to the four different *Jerlov* [1976] water types. See also Table 1 for explanations.

The vertical mixing velocity ω_m is determined using a modified version of the Kraus-Turner (KT) model [*Kraus and Turner*, 1967; *Niiler and Kraus*, 1977] as given by *Rochford et al.* [2000]. The terms in the total kinetic energy (TKE) budget (*P*) are parameterized as follows:

$$P = (m_3 - m_1)u_*^3 - h_m \left(\frac{1}{2}n_c u_* b_* - \epsilon_b + m_5 \widehat{f} u_*^2\right), \quad (10)$$

$$u_*^2 = \frac{|\tau_a|}{\rho_o}, \quad (11)$$

$$u_* b_* = \frac{g\alpha(T_m)Q_{abs}(h_m)}{\rho_o C_{pw}}, \quad (12)$$

$$\epsilon_b = \begin{cases} m_6 u_* b_* & u_* b_* < 0 \\ 0 & u_* b_* \geq 0, \end{cases} \quad (13)$$

$$\widehat{f} = \max[|2\Omega\sin(\phi)|, f_*]. \quad (14)$$

When turbulent mixing is shallowing (i.e., $P < 0$), mixing occurs toward the equilibrium depth as given by

$$h_m^* = \frac{(m_3 - m_1)u_*^3}{\frac{1}{2}n_c u_* b_* - \epsilon_b + m_5 \widehat{f} u_*^2} \quad (15)$$

$$\omega_m = \sigma_\omega \left[\max\left(h_m^*, h_m^+\right) - h_m\right] \quad (16)$$

while when it is deepening (i.e., $P > 0$), the available TKE is converted to potential energy via

$$\omega_m = \frac{P}{g\alpha(T_m)\max(\Delta T_b, \Delta T_b^+) h_m} \quad (17)$$

$$\Delta T_b = (T_m - \Delta T_m) - T_b. \quad (18)$$

A minimum value is imposed on the MLD ($h_m^+ = 10$ m, see (16)) because the formulation is not accurate for very shallow mixed layers. The reader is referred to Appendix B for the various parameters and their values.

A temperature profile is constructed from the SST, layer temperatures, the temperature change across the mixed layer (ΔT_m), and other layer quantities. This is used to estimate the temperature shear at the base of the mixed layer (ΔT_b), and the temperature of the entrained water (T_b). This includes new formulations for prescribing ΔT_b and T_b as well as specifying ΔT_m as a function of latitude from climatological data.

The model domain is identical to that used by *Shriver and Hurlburt* [1997], which includes the global ocean at all longitudes from 72°S to 65°N, gridded to a resolution of 0.5° latitude and 0.703125° longitude (NLOM W125 domain). The lateral boundaries follow the 200 m isobath contour, and six active layers (*n* = 6) are used for the simulations reported here. The time step used in the model is $\Delta t = 36$ min. A complete list of the values used for the model parameters is given in Appendix B and Table 2.

3.2. Subsurface Heating

The downward total incoming solar irradiance (Q_{SOL}) and upward outgoing longwave radiative flux (Q_{LW}) at the ocean surface are prescribed as by *Rochford et al.* [2000], namely, using the monthly fields from the Comprehensive Ocean-Atmosphere Data Set (COADS) [*Da Silva et al.*, 1994]. For the downward latent and sensible heat fluxes (Q_E and Q_S, respectively) we explicitly calculate them using the OGCM SST (T_m):

$$Q_E = C_L L_v \rho_a \widetilde{v}_a (q_a - q_m), \quad (19)$$

$$Q_S = C_S C_{pa} \rho_a \widetilde{v}_a (T_a - T_m), \quad (20)$$

$$\rho_a = \frac{100 P_a}{[R_{gas}(T_a + 273.16)]}, \quad (21)$$

$$q_a = \frac{0.622 e_s(T_d)}{P_a - 0.378 e_s(T_d)}, \quad (22)$$

$$q_m = 0.98 \, q_{sat}(T_m), \quad (23)$$

$$q_{sat}(T) = 0.62197 \sum_{l=0}^{6} q_l \, T^l, \quad (24)$$

$$e_s(T) = 6.1121 \, (1 + 3.46 \times 10^{-6} P_a)\exp[17.5T/(240.97 + T)], \quad (25)$$

Table 2. Layer-Dependent NLOM Parameter Values

Parameter	*k*					
	1	2	3	4	5	6
H_k, m	80	160	260	400	600	5000
h_k^+, m	50	40	40	40	40	
h_k^-, m	9999	9999	9999	9999	9999	9999
ω_k, m s^{-1}	0.1	0.1	0.1	0.1	0.1	0.1
$\Delta\rho_k^+$, kg m^{-3}	0.4	0.3	0.2	0.1	9.9	

where the exchange coefficients C_S and C_L are as given by *Kara et al.* [2000a], $\tilde{v}_a$ is the wind speed as determined via the prescription given by *Kara et al.* [2000a], and T_a (q_a) is the COADS air temperature (humidity). For the model simulations reported here, the wind speed v_a used to determine $\tilde{v}_a$ is extracted from the applied wind stress magnitude τ (see section 4.1) by inverting the relation

$$\tau = \rho_a C_d v_a^2 \qquad (26)$$

using a constant value of $\rho_a C_d = 1.8 \times 10^{-3}$ kg m^{-3}. We explicitly calculate Q_E and Q_S in this manner because they serve as restoring terms for relaxing the SST to within 1–3°C of the air temperature [*Rochford et al.*, 2000] and avoid the well-known problem of SST drift when forcing an OGCM with prescribed net surface heat fluxes. This approach has been found to work reasonably well when using the COADS fields [*Rochford et al.*, 2000].

We include the attenuation of the solar irradiance with ocean depth z by first decomposing the surface solar irradiance Q_{SOL} into its infrared and PAR components ($Q_{SOL} = \text{IR}(z) + \text{PAR}(z)$, where $z = 0$). The net surface heat flux $Q_{abs}(z)$ that has been absorbed (or lost) by the upper ocean to depth z is then the sum

$$Q_{abs}(z) = \text{IR}(0) - \text{IR}(z) + \text{PAR}(0) - \text{PAR}(z) - Q_{LW} + Q_E + Q_S, \qquad (27)$$

where IR(z) [PAR(z)] is the infrared irradiance [PAR] at depth z. No depth dependence is assigned to the last three components because the heat exchange is locally confined to the air-sea interface. *IR* and *PAR* can be expressed as fractions of the solar irradiance Q_{SOL},

$$\text{IR}(0) = (1 - \lambda_{PAR})Q_{SOL} \qquad (28)$$

$$\text{PAR}(0) = \lambda_{PAR}Q_{SOL}, \qquad (29)$$

with λ_{PAR} (in general) having a dependence on space and time. Given that the IR component is absorbed within the first few centimeters and that this is much less than the minimum MLD imposed in most OGCM (e.g., 5–10 m), all of the IR solar irradiance arriving at the air-sea interface can be considered to be heating the upper ocean, i.e., IR(z) = 0 for $z > 10$ cm. Using these relations along with the exponential attenuation of PAR with depth (2), one obtains as the heat absorbed within the upper water column to depth z:

$$Q_{abs}(z) = Q_{NET} - \lambda_{PAR}Q_{SOL} \exp(-k_{PAR}\,z), \qquad (30)$$

where

$$Q_{NET} = Q_{SOL} - Q_{LW} + Q_E + Q_S \qquad (31)$$

is the net surface heat flux at the ocean surface. The rate of surface heating/cooling of the mixed layer is simply obtained by evaluating this expression at the MLD (i.e., $z = h_m$).

We apply a PAR that is constructed from the surface solar irradiance as given by (29). While SeaWiFS PAR Level 3 standard mapped images are now available (daily, 8 day, and monthly means) these products do not contain additional statistical information such as the number of images contributing to the temporal mean at a given location. This prevents the proper construction of a monthly climatology of SeaWiFS PAR from the multiple years of monthly means. Furthermore, when comparing our PAR derived from COADS against the monthly means of SeaWiFS PAR for different years we find differences ≤ 25 W m^{-2}. This difference in PAR is insufficient to produce an appreciable change in the OGCM simulation. For these reasons we elect to apply (29) to be consistent with the surface heat flux forcing being applied to our OGCM (see section 4.1). This is trivial to implement and is an approach that would be

commonly pursued by other ocean modelers for climatological studies. In studies investigating interannual variations, and unique events such as ENSO, the use of SeaWiFS PAR in the surface forcing for the OGCM would be invaluable.

To specify the PAR fraction of the solar irradiance at the sea surface (λ_{PAR}), we make use of the *Bishop and Rossow* [1991] monthly climatologies of PAR and surface solar irradiance made available from the SeaWiFS Project at NASA GSFC (data set ds741.0, Bishop's Surface Solar Irradiance derived from International Satellite Cloud Climatology Project (ISCCP)). The 2.5° × 2.5° monthly climatologies of PAR and Q_{SOL} span the global ocean at all longitudes from 88.75°S to 88.75°N. The climatologies were constructed using data from ISCCP collected from July 1983 to June 1991 and validated against time series of radiance observations from moorings in the northeastern Pacific Ocean [*Bishop and Rossow*, 1991]. The combined average bias from that study was found to be only 5 W m^{-2}, with a worst case error of <7% for clear sky irradiance, making it a reliable data source for the determination of λ_{PAR}.

In determining λ_{PAR} for modeling purposes it is important to consider whether there are significant temporal or spatial variations in this quantity. Specifically, whether there is a significant seasonal variability and whether there is a significant latitude variability given the meridional nature of surface irradiance. A histogram constructed from the ratios of PAR/Q_{SOL} obtained from the climatology data for the middle months of the four seasons (Figure 3) reveals λ_{PAR} varies from 0.33 to 0.50 over the global ocean, with the distribution strongly skewed to the larger values. While the PAR/Q_{SOL} distributions vary appreciable from month to month, the median value remains almost constant. For all 12 months of the climatology the median of the monthly distributions vary by at most 0.3%. The median value and standard deviation for the distribution composed of all 12 months is 48 and 2%, respectively.

As for spatial variation, we find that λ_{PAR} does have a small meridional dependence, with the ratios from the entire climatology yielding a normal distribution centered at the equator (Figure 4). This meridional dependence from $\phi = 40°$S to 40°N can be expressed as a simple quadratic function obtained via a least squares fit: $\lambda_{PAR} = 0.4973 + 2.941 \times 10^{-5}\,\theta - 1.242 \times 10^{-5}\,\theta^2$, where θ is the latitude in degrees. Given that the monthly and meridional variation in PAR/Q_{SOL} is so small, we choose to use the constant value $\lambda_{PAR} = 0.49$ for all the NLOM simulations. This is slightly larger than the median value of 48.15% for the entire monthly climatology because we expect low latitudes to be particularly important. Note that this choice also yields a comparable absorption profile to those of Jerlov for the k_{PAR} values we have chosen for the Jerlov water classes (see Figure 2).

For our present application the greatest interest is in those situations where subsurface heating can occur below the mixed layer, thereby resulting in a cooler SST than obtained by assuming complete absorption of solar irradiance within the OGCM mixed layer. Accounting for this decreased heating in the OGCM mixed layer will also influence the buoyancy forcing and may thereby significantly alter the MLD. Such subsurface heating occurs when there is high surface PAR, large optical depths (e.g., $k_{PAR}^{-1} \geq 20$ m), and a shallow mixed layer. The surface PAR obtained using $\lambda_{PAR} = 0.49$ and the COADS solar irradiance are therefore shown for the middle months of the four seasons in Plates 3 and 4. The surface PAR fields from COADS are found to be quite similar to the pattern of the k_{PAR} fields derived from SeaWiFS (Plates 1 and 2).

From the monthly PAR (Plates 3 and 4) and monthly k_{PAR} (Plates 1 and 2) we observe that strong solar heating occurs in conjunction with optical depths of the order of 15–20 m throughout the year in the 10°S–10°N equatorial belt of the Pacific. Strong surface PAR also occurs with somewhat shallower optical depths of 14–17 m in the Arabian Sea during the
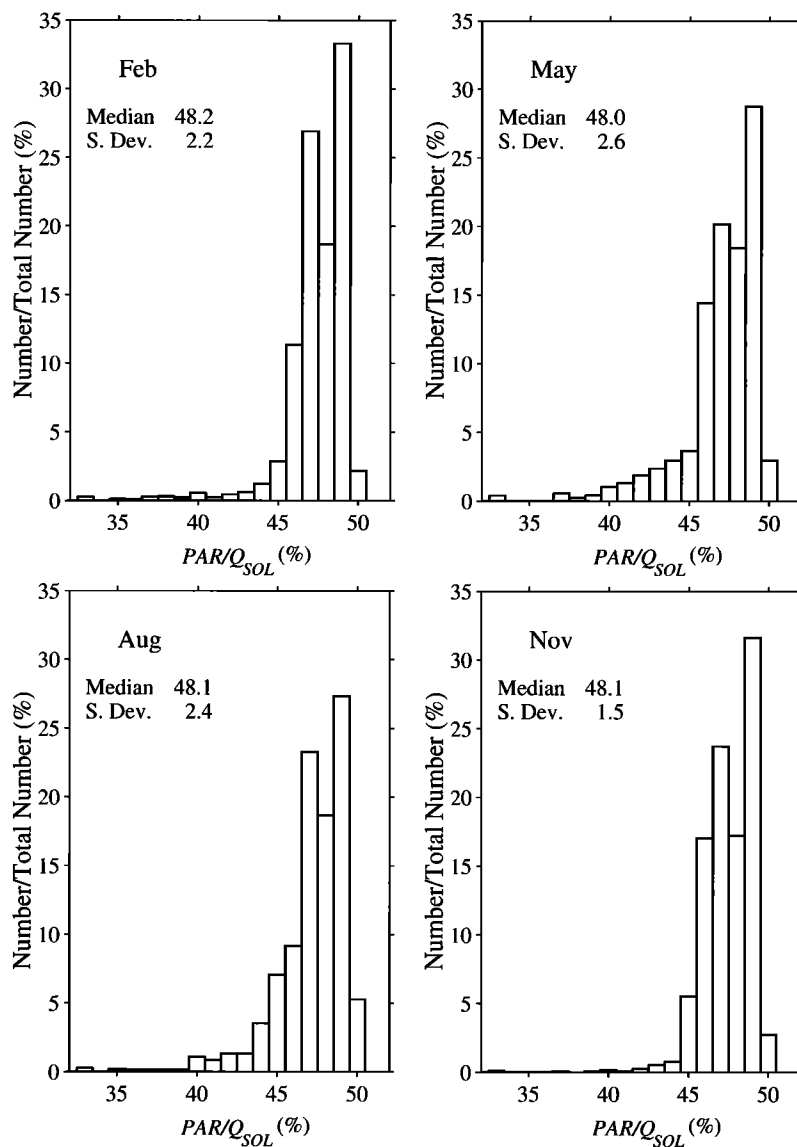
Figure 3. The statistical distribution of the ratio of PAR to total surface irradiance (Q_{SOL}) from the monthly climatology of *Bishop and Rossow* [1991] for the middle months of the four seasons. The median and standard deviation (S. Dev.) values are also shown. Statistics are binned in PAR/Q_{SOL} increments of 1%. The distributions for the 4 months shown reveal PAR/Q_{SOL} ranges mostly from 46 to 50% over the global ocean.

spring intermonsoon (May k_{PAR}, Plate 1), with similar results occuring in the fall intermonsoon (October k_{PAR}, not shown). An MLD ≤ 10 m is known to occur in the equatorial Pacific throughout the year [*Anderson et al.*, 1996] and in the Arabian Sea during the intermonsoon periods of mid-February through May and mid-September through mid-October (R. A. Weller, private communication, 1998). These are therefore two regions where subsurface heating is expected to have a large impact on SST and MLD and will be particular regions of focus later on in this study.

4. Effect of Subsurface Solar Heating

4.1. Model Simulations

All NLOM simulations reported here are surface forced with monthly mean climatologies to obtain a climatological solution.

This is done because we wish to assess the consequence of subsurface heating without bias to atmospheric forcing of a particular time period. For NLOM wind stress forcing we use 12-hourly anomalies from the European Centre for Medium-Range Weather Forecasts (ECMWF) operational weather forecast model [*ECMWF*, 1993, 1997], with the monthly varying seasonal cycle of the monthly mean wind stress climatology of *Hellerman and Rosenstein* [1983] (hereinafter referred to as HR). We use the winds from September 1994 through September 1995, inclusive, to construct the 12-hourly ECMWF wind anomalies with the 12-hourly September 1994 and September 1995 wind stresses blended to make a complete annual cycle. We choose this period because the winds represent an "average" annual cycle of the ECMWF winds and because the September winds in 1994 and 1995 most closely match each other. With these hybrid winds the long-term temporal mean is driven by the HR monthly wind stress, while the variability is
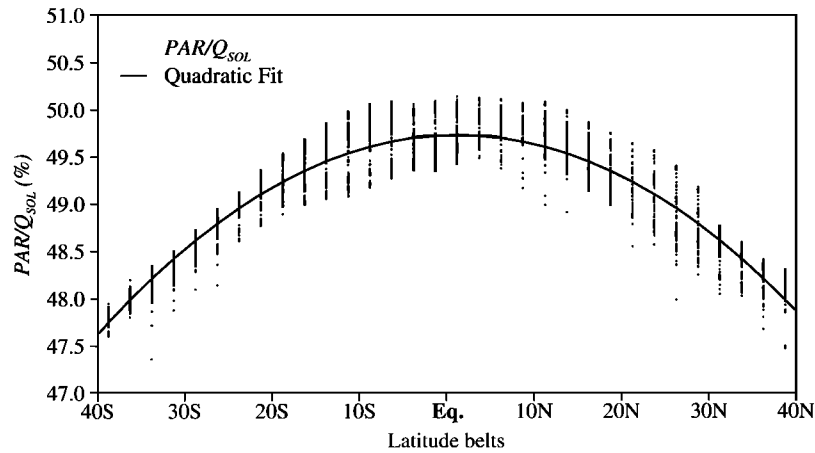
Figure 4. Zonally averaged percentage PAR/Q_{SOL} values between 40°S and 40°N over the global ocean. The data are plotted at the 2.5°latitude increments of the *Bishop and Rossow* [1991] climatology. A quadratic fit is found as the best estimation of zonally averaged PAR/Q_{SOL} values for the latitude range (θ) shown: $\lambda_{PAR} = 0.4973 + 2.941 \times 10^{-5}$ $\theta - 1.242 \times 10^{-5} \theta^2$.

driven by ECMWF component and flow instabilities. When the NLOM is forced with the pure HR monthly wind stresses rather than the hybrid wind stresses, SST predictions over the global ocean became weak and exhibited a large bias, indicating the importance of using wind stresses of high temporal resolution (e.g., 6 or 12 hourly). Use of the hybrid winds also eliminated unrealistic current patterns in some regions and has been successfully used in other ocean modeling studies [*Metzger et al.*, 1992; *Hurlburt et al.*, 1996; *Shriver and Hurlburt*, 1997; *Hurlburt and Metzger*, 1998]. We omit here the details regarding the construction of this climatology for brevity and because they will be reported in the future paper on this version of the NLOM.

For the heat flux forcing the monthly climatologies of COADS are used [*Da Silva et al.*, 1994] as described in section 3.2 to be consistent with the hybrid wind forcing in producing a climatological solution. Using COADS instead of HR monthly wind stress in a test simulation with the Indian Ocean NLOM yielded only minor differences. The COADS thermal forcing includes shortwave (incoming solar) plus longwave radiation ($Q_{SOL} + Q_{LW}$), air temperature T_a at 10 m, and the air mixing ratio q_a at 10 m. The latent and sensible heat fluxes are explicitly calculated using mixed layer temperature T_m at the model time step (see section 3.2) to serve as a restoring term that relaxes the SST to the air temperature. In all experiments the surface PAR is applied as formulated in section 3, i.e., $\lambda_{PAR} = 0.49$ in (29).

The NLOM is spun up to statistical energy equilibrium, and this spin-up time is ~500 years. The model run is then extended for 5 years with an active mixed layer. Because our model simulations are performed using climatological forcing as described above, the monthly means of model SST are formed from January through December of the fifth year with an active mixed layer. This is done so that model-data comparisons can be made.

To determine the consequences of subsurface heating on SST and MLD prediction, we performed three experiments using the NLOM. The first is a baseline experiment where we set $k_{PAR} = 99$ m^{-1} so the surface PAR is completely absorbed within the mixed layer. It is representative of traditional OGCM approaches that assume a complete absorption of solar irradiance at the ocean surface [*Baturin and Niiler*, 1997; *Carton and Zhou*, 1997; *Murtugudde et al.*, 1995; *Schopf and Loughe*, 1995; *Sterl and Kattenberg*, 1994; *Yuen et al.*, 1992]. We will refer to this as the "large k_{PAR}" experiment (NLOM W125 experiment 39.4). The

second experiment accounts for the seasonal and spatial variation of subsurface heating by using the monthly k_{PAR} data set introduced in section 2. We label this the "monthly k_{PAR}" experiment (NLOM W125 experiment 38.8). The third experiment uses a global constant value of $k_{PAR} = 0.06$ (NLOM W125 experiment 39.3), which is representative of clear water open ocean conditions (see section 2). The rationale for this "clear water k_{PAR}" experiment will be given below after the SST results from the above two experiments have been presented.

4.2. SST

The impact of including subsurface heating in the NLOM is expected to be most evident in the difference in SST from the monthly k_{PAR} experiment relative to the SST from the large k_{PAR} experiment. This is most easily seen over the global domain from an annual mean of the SST difference ($\overline{\Delta SST}$) between the two experiments (Plate 5a) using the SST from the fifth year of the NLOM simulations with an active mixed layer. We calculated this annual mean by forming the monthly mean SST for each experiment, taking the differences month by month between the two experiments, and then calculating the annual mean of these differences. While such annual means can mask large SST differences that may occur during the year because it averages over the annual cycle (see ΔSST in Figure 5), the nonzero differences that remain are sufficient to identify the importance of subsurface heating in the various regions of the global ocean.

Neglect of subsurface heating is seen to produce an annual mean SST increase that is on the order of at most 0.2°–0.8°C, and that is predominantly confined to the 40°S–40°N latitude region. These differences reflect changes in seasonal variability that can be as large as 1°–1.5°C (Figure 5). The magnitude of the seasonal variability in SST is comparable to that obtained with one-dimensional mixed layer models [*Kantha and Clayson*, 1994]. The NLOM SST increase in the low and midlatitudes overlaps with the region of optical depths ranging from $14 \leq k_{PAR}^{-1} \leq 20$ m (see Plates 1 and 2). These optical depths are greater than the typical NLOM MLD (~5–10 m) for this region. A colder SST results in the monthly k_{PAR} experiment because only a fraction of the total surface PAR is absorbed in the mixed layer. The regions of largest positive values of $\overline{\Delta SST}$ (~1°C) are in the western equatorial Pacific, the equatorial Indian Ocean, and the northern low-latitude
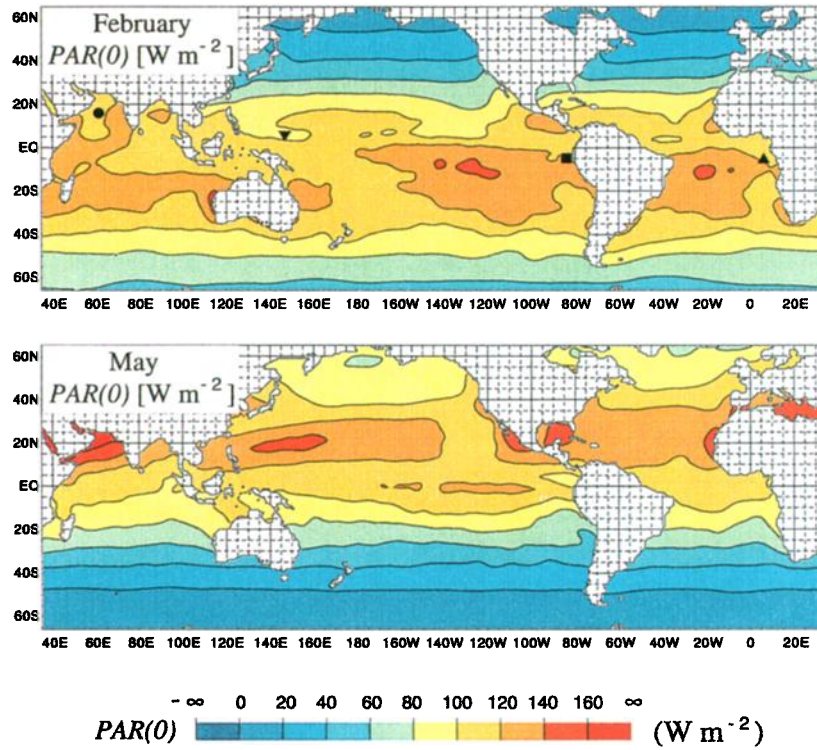
Plate 3. PAR at the ocean surface obtained from Comprehensive Ocean-Atmosphere Data Set (COADS) for the middle month of the Northern Hemisphere winter (February) and spring (May). The global coverage is from 72°S to 65°N of the NLOM domain. The black circle, triangle, square, and inverted triangle in the top panel indicate the locations of the time series in Figures 1 and 5.
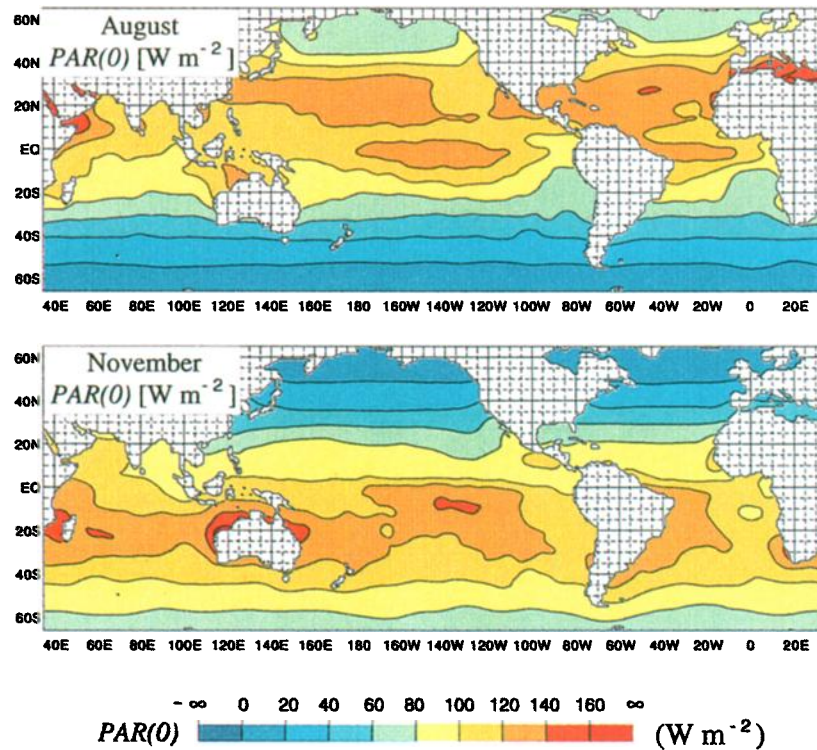

Plate 4. The same as Figure 3 but for the middle month of the Northern Hemisphere summer (August) and fall (November).
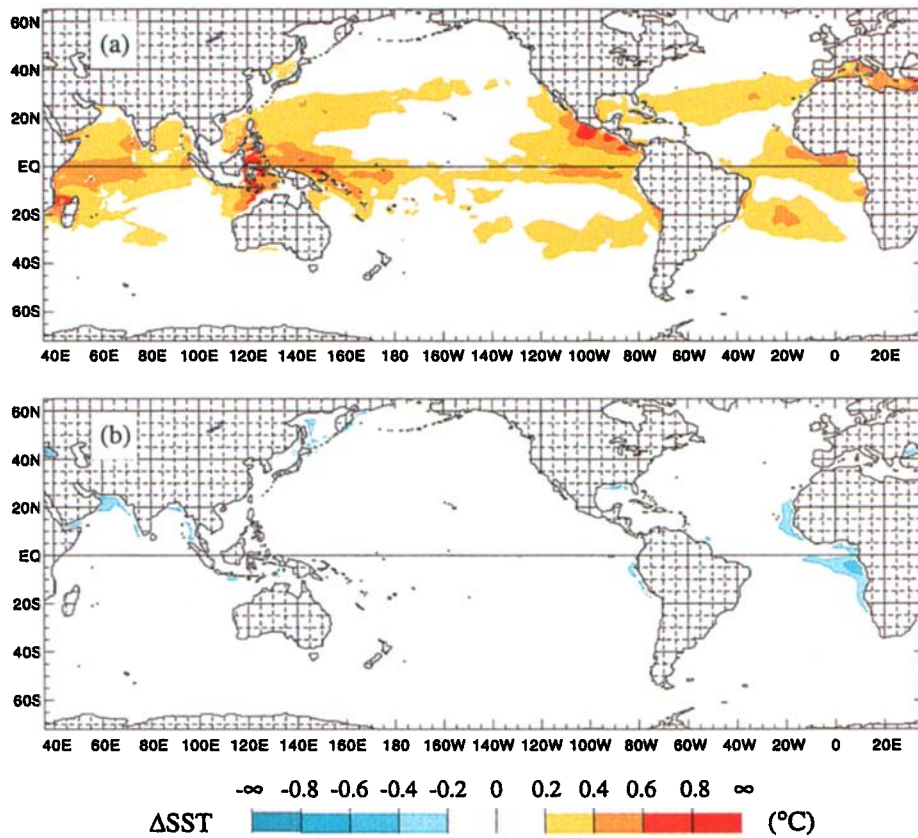
Plate 5. Annual mean of SST difference ($\overline{\Delta SST}$) between NLOM experiments. (a) SST when all the radiation is absorbed within the mixed layer (large k_{PAR} experiment) minus the SST when using a monthly varying k_{PAR} (monthly k_{PAR} experiment). (b) SST when using $k_{PAR} = 0.06$ m^{-1} (clear water k_{PAR}) minus the SST when using a monthly varying k_{PAR} (monthly k_{PAR} experiment).
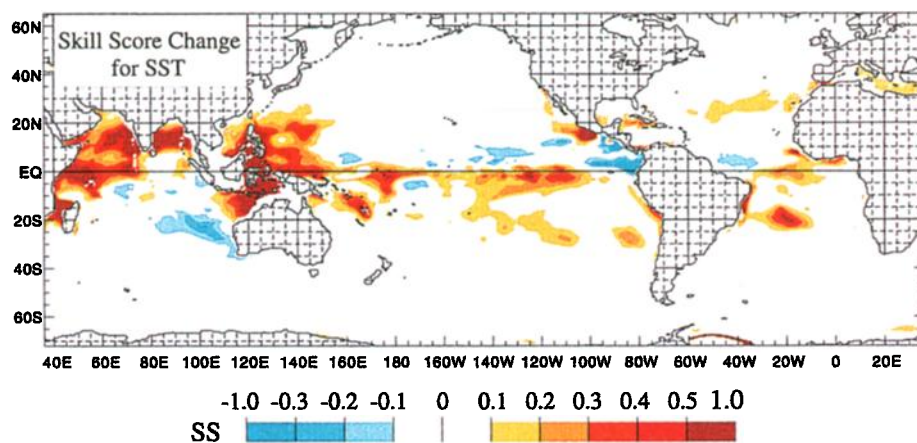

Plate 6. The nondimensional skill score (SS) for the monthly k_{PAR} SST minus the SS for the large k_{PAR} SST (Δ SS). The SS for each experiment is determined from the monthly mean SST relative to the monthly SST from COADS. The positive values of $\Delta SS \geq 0.1$ indicate the increase in SST predictive skill of the NLOM when including subsurface heating using the monthly k_{PAR}.
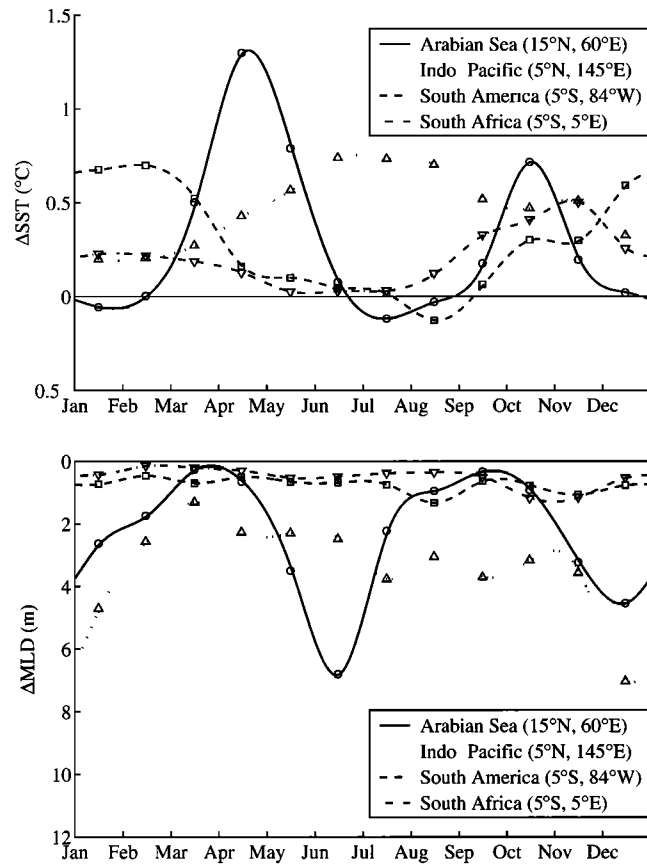
Figure 5. Time series of the difference in monthly SST (ΔSST) and monthly MLD (ΔMLD) between two NLOM experiments at four selected sites in the global ocean (see Figure 1 for k_{PAR} values). Shown are the results when all the radiation is absorbed within the mixed layer (large k_{PAR} experiment) minus the results when using a monthly varying k_{PAR} (monthly k_{PAR} experiment). The locations of the time series are indicated in the top panel of Plate 3 according to the geometric symbols on the above lines.

eastern Pacific. When using an optimal MLD definition [*Kara et al.*, 2000b], these regions are found to retain a fairly shallow climatological MLD (~20–40 m) throughout the year and to coincide with a large seasonal variability in k_{PAR} (Figure 1).

To determine if subsurface heating improves the SST predictive skill of the NLOM, we calculate a nondimensional skill score [*Murphy*, 1995] for the SST of the two simulations relative to the SST from the COADS monthly climatology at each model grid point over the Global Ocean. The skill score is given by

$$SS(x,y) = 1 - \frac{RMSE(x,y)^2}{\sigma(x)^2} \qquad (32)$$

where $RMSE(x, y)$ is the root-mean-square error between x and y and $\sigma(x)^2$ is the variance of the 12 monthly reference values. In the present case, x and y are the time series of monthly mean SST fields from COADS and the NLOM experiments, respectively, at each grid point from January to December (i.e., $n = 12$). All of the 12 monthly means are used in the determination of the SS. A positive value for SS indicates a good forecast. This provides a quantitative measure of how well the NLOM SST reproduces the seasonal SST cycle. Regions where positive values occur in the difference between these skill

scores (monthly k_{PAR} minus large k_{PAR} SS) indicate an improvement in NLOM SST prediction when subsurface heating is included. Values of $\Delta SS \geq 0.1$ indicate an increase in predictive skill. The SS difference (Plate 6) reveals that the inclusion of subsurface heating improves NLOM SST predictive skill in the equatorial regions and markedly increases this skill in the Arabian Sea, the Bay of Bengal, and the shallower Indonesian Pacific. The regions of $\Delta SS < 0$ are confined to isolated areas of smaller extent and are smaller in magnitude than the areas of $\Delta SS > 0$. While the annual mean difference in SST may be small, the positive increases in SS of 0.3–0.5 clearly indicate that NLOM SST prediction is significantly improved by including subsurface heating.

The improvement in NLOM SST prediction that results from including subsurface heating is observed to be mostly confined to regions where the NLOM MLD is <20 m. This is not surprising because of the rapid attenuation with depth ($k_{PAR}^{-1} \leq 17$ m) over most of the global ocean. However, it does suggest that a constant value of k_{PAR} that is representative of maximum light penetration over most of the open ocean may be adequate for OGCM applications. To test this assumption, we perform an experiment with a fixed value of $k_{PAR} = 0.06$ m^{-1} that is indicative of clear water open ocean conditions in the monthly k_{PAR} data set (see Plates 1 and 2). The $\overline{\Delta SST}$ for the clear water k_{PAR} experiment relative to the monthly k_{PAR} experiment is found to be <0.2°C over most of the global domain (Plate 5b). Larger differences of up to 0.6°C only occur in limited regions and primarily at low latitudes, where the monthly k_{PAR} shows that strong optical attenuation is prevalent throughout the year (see Figure 1). These regions of large $\overline{\Delta SST}$ are the northern Arabian Sea and the Sea of Okhotsk and along the western coast of South America and off the western coast of Africa. Unless one is using an OGCM to model ocean dynamics in these regions, most notably the northern Arabian Sea and along the western coast of Africa, a global constant value of $k_{PAR} = 0.06$ m^{-1} will serve very well.

4.3. MLD

A change in depth of the NLOM embedded mixed layer is expected given the observed changes in SST that occur upon including subsurface heating. The question is how large a change in MLD does subsurface heating produce, and is it of sufficient magnitude to be significant in an OGCM? As with the SST, this is most easily seen from an annual mean of the MLD difference ($\overline{\Delta MLD}$) between pairs of experiments. The $\overline{\Delta MLD}$ for the large k_{PAR} experiment relative to the monthly k_{PAR} experiment (Plate 7a) reveals that neglect of subsurface heating produces a shallowing of the mixed layer in the range of 1–4 m over the low and middle latitudes (40°S–40°N). These differences reflect modest changes in seasonal variability of 1–6 m (Figure 5).

The deeper MLD in the monthly k_{PAR} experiment relative to the large k_{PAR} experiment is because of the lower buoyancy produced in the former relative to the latter. An increase in surface heating produces more positive buoyancy and thereby a shallower mixed layer. Less positive buoyancy is produced when the surface solar irradiance can penetrate beneath the mixed layer, and thus a deeper mixed layer results. The deepening of only a few meters relative to typical mixed layer depths of 40–80 m tells us that subsurface heating is not important for OGCM prediction of MLD. To influence the depth of the mixed layer, k_{PAR} must be very large, and MLD must be very shallow. This is confirmed by the skill scores calculated for the monthly means of these MLD relative to a MLD formed from monthly temperature and salinity climatologies [*Levitus and Boyer*, 1994; *Levitus et al.*, 1994] using an optimal MLD definition [*Kara et al.*, 2000b]. The skill score difference between any two experiments is less than the threshold criteria for skill score significance ($\Delta SS \leq 0.1$) throughout the global domain (results not shown).
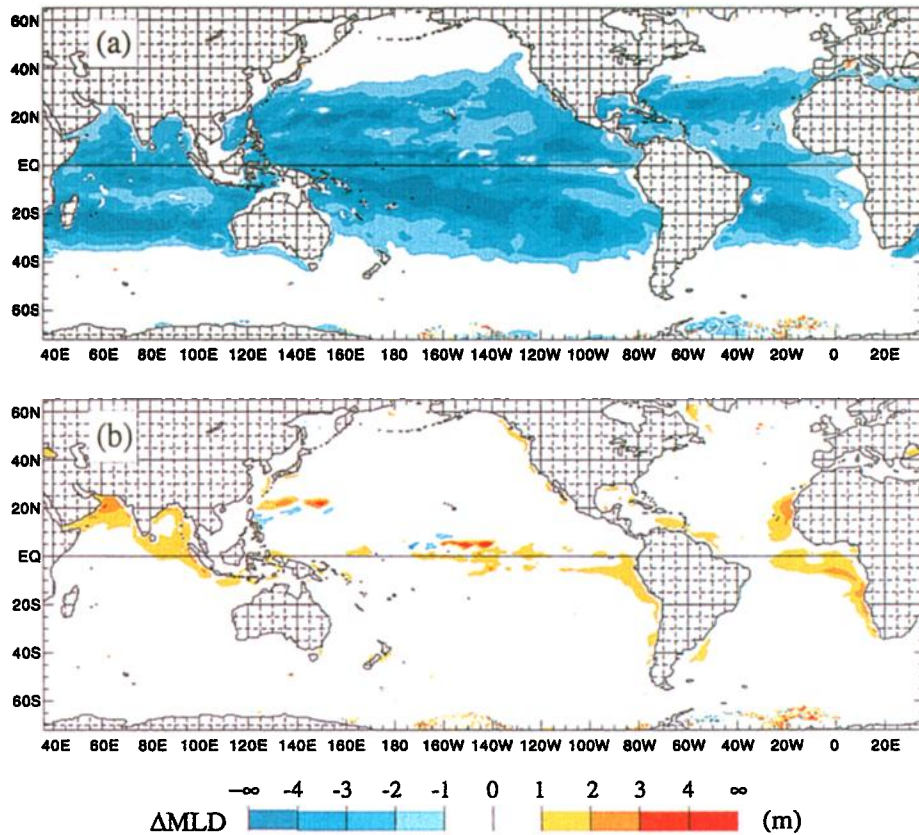
Plate 7. Annual mean of MLD difference $\overline{\Delta MLD}$ between NLOM experiments. (a) MLD when all the radiation is absorbed within the mixed layer (large k_{PAR} experiment) minus the MLD when using a monthly varying k_{PAR} (monthly k_{PAR} experiment). (b) MLD when using $k_{PAR} = 0.06$ m^{-1} (clear water k_{PAR}) minus the MLD when using a monthly varying k_{PAR} (monthly k_{PAR} experiment).

The $\overline{\Delta MLD}$ for the clear water k_{PAR} experiment relative to the monthly k_{PAR} experiment (Plate 7b) reveals the mixed layer deepens by 1–3 m over limited regions of the globe. Most of these regions overlap with those observed for $\overline{\Delta SST}$ (Plate 7b). Regions for which there is no $\overline{\Delta SST}$ compliment are the western Pacific region east of China, the central equatorial Pacific, and along the western coast of North America. The deeper mixed layer occurs when using the monthly k_{PAR} versus $k_{PAR} = 0.06$ m^{-1} for the same reason as the warmer SST, namely, a greater absorption of the surface irradiance within the mixed layer because of stronger optical attenuation. The limited regions for which there are differences between these two experiments combined with their typically small magnitude of $\Delta MLD \leq 3$ m confirm that a global constant value of $k_{PAR} = 0.06$ m^{-1} will serve well enough for general global modeling purposes.

5. Conclusion

From this investigation we find that inclusion of solar subsurface heating in the NLOM with an embedded mixed layer is important for improving the model prediction of SST in the equatorial regions of the world ocean. We showed that accounting for the seasonal variation of solar attenuation with depth to be particularly important for SST prediction in the Arabian Sea, Bay of Bengal, and Indonesian Pacific regions. Differences of as much as 0.8°C in the annual mean SST occur when accounting for subsurface heating versus its complete neglect. Subsurface

heating was not important for MLD prediction in the NLOM, as it produced a deepening of only a few meters in the mixed layer. Although the importance of subsurface heating was already known from earlier one-dimensional modeling studies, those findings were not studied in detail. The results presented here quantify for the first time its importance for ocean general circulation model global simulations.

In conducting this study we also constructed a global data set of monthly mean k_{PAR} suitable for use in an OGCM and employed it to prescribe the attenuation of surface irradiance with depth within the NLOM. This data set represents one of the first applications of remotely sensed observations from SeaWiFS that have been used to enhance an OGCM simulation. Through its use we have shown that a constant value of $k_{PAR} = 0.06$ m^{-1}, which is indicative of open ocean conditions, works very well for most global OGCM applications of interest, a result that would have been unjustified without the use of such a data set. Having this data set now opens up the possibility to represent seasonal subsurface light conditions in a variety of applications for mixed layer and biophysical models embedded within an OGCM. It is our hope this k_{PAR} data set will find wider use for such OGCM applications.

Finally, we note this study was limited to examining the effects of solar subsurface heating over the global ocean using monthly forced climatological simulations. In a future paper we shall present results from a study of interannual variability, with a particular focus on the equatorial region where solar subsurface

heating is found to be important, as well as other regions where climatological simulations may not account for the importance of a space- and time-varying k_{PAR} field. We believe the specific findings we have obtained here for the NLOM extend to other global OGCM with embedded mixed layers.

Appendix A: Statistical Interpolation of k_{490}

Statistical interpolation (SI) is a minimum variance method that seeks to minimize the expected error in the analysis field [Daley, 1991; Lorenc, 1981]. The method determines an interpolated analysis field value f_A at a location r_i from a weighted sum of known observed and background field values f_O and f_B, respectively, at other locations (r_j, $j = 1, \ldots, n$; $r_j \neq r_i$) via

$$f_A(\mathbf{r}_i) = f_B(\mathbf{r}_i) + \sum_{j=1}^{n} W_{ij}[f_O(\mathbf{r}_j) - f_B(\mathbf{r}_j)], \qquad (A1)$$

where W_{ij} is a covariance weight vector for the location r_i [Daley, 1991, equation (4.2.9)]. Since there are no in situ observations for the mean k_{490}, we have $f_O = 0$. Similarly, $f_B(r_i) = 0$ because we have no background value at r_i. The weight vector is determined by solving the matrix equation

$$\sum_{k=1}^{n} B_{jk}W_{ki} = C_{ji}, \qquad (A2)$$

where

$$B_{jk} = \langle \Delta f_B(\mathbf{r}_j)\Delta f_B(\mathbf{r}_k) \rangle \qquad (A3)$$

$$C_{ji} = \langle \Delta f_B(\mathbf{r}_j)\Delta f_B(\mathbf{r}_i) \rangle \qquad (A4)$$

are the covariances in the field value errors Δf_B. The $n \times n$ symmetric matrix B is the error covariance matrix among the background field values at the noninterpolated locations ($j, k = 1, \ldots, n$), and the n vector C is the corresponding error covariance vector of the background field values at noninterpolated locations with respect to the interpolated location [Daley, 1991, equation (4.2.10)]. For lack of information on the root-mean-square errors of the mean k_{490}, the covariances are assigned correlation functions of

$$B_{jk} = \exp[-|\mathbf{r}_j - \mathbf{r}_k|/r_0] \qquad (A5)$$

$$C_{ji} = \exp[-|\mathbf{r}_j - \mathbf{r}_i|/r_0], \qquad (A6)$$

with a distance scale of $r_0 = 1°$. The value of r_0 was chosen to be consistent with the grid resolution.

The data filling of the SeaWiFS k_{490} using SI proceeds by searching for data voids along latitude transects starting from the equator and moving poleward in alternating north-south latitudes. Searches along longitude proceed from west to east and then from east to west. An interpolating grid box of 5 × 5 centered at the data void is used for the SI in all but the last 2 latitude rows at the poleward boundaries. A 3 × 3 box is used for the second last rows, and a 3 × 2 box is used for the boundaries. Data voids at noncentral locations in the interpolating box are excluded when performing the SI.

Appendix B: NLOM Notation

B.1. Definitions

We list here the mathematical definitions of various quantities appearing in the NLOM equations.

$$G_{kl} = \begin{cases} g & l \geq k \\ g - g(\rho_k - \rho_l)/\rho_o & l < k \end{cases} \qquad (B1)$$

$$H_n = D(x,y) - \sum_{l=1}^{n-1} H_l \qquad (B2)$$

$$\tau_k = \begin{cases} \tau_a & k = 0 \\ 0 & k = 1 \ldots n-1 \\ C_b\rho_o|\mathbf{v}_n|\mathbf{v}_n & k = n \end{cases} \qquad (B3)$$

$$\omega_k = \begin{cases} \widehat{\omega}_e & k = 0 \\ \omega_k^+ - \omega_k^- - (\overline{\omega_k^+ - \omega_k^-})\,\Omega_k\,/\,\overline{\Omega}_k & k = 1 \ldots n-1 \\ 0 & k = n \end{cases}$$

$$\qquad (B4)$$

$$\omega_1^+ = \tilde{\omega}_1\{\max[0, (h_m + h_1^+ - h_m^+) - h_1]/h_1^+\}^2 \qquad (B5)$$

$$\omega_k^+ = \tilde{\omega}_k[\max(0, h_k^+ - h_k)/h_k^+]^2 \qquad k \geq 2 \qquad (B6)$$

$$\omega_k^- = \tilde{\omega}_k[\max(0, h_k - h_k^-)/h_k^+]^2 \qquad k \geq 2 \qquad (B7)$$

$$\Delta\rho_k = \max(\rho_{k+1} - \rho_k - \Delta\rho_k^+, 0) \qquad (B8)$$

Note that $\overline{\omega_k^+ - \omega_k^-}$ and $\overline{\Omega}_k$ denote area averages of the respective quantities over the ocean model domain.

B.2. Notation

We list here the symbols appearing in the NLOM equations that are not defined elsewhere in the manuscript.

A_H coefficient of horizontal eddy viscosity (1500 $m^2 s^{-1}$).

C_b coefficient of bottom friction (0.002).

C_M coefficient of additional interfacial friction on entrainment.

C_{pa} specific heat capacity for air (1004 J kg^{-1} $°C^{-1}$).

C_{pw} specific heat capacity for water (3988 J kg^{-1} $°C^{-1}$).

$D(x, y)$ total depth of the ocean at rest.

e_s saturated vapor pressure.

f Coriolis parameter.

f_* Coriolis parameter at 5° latitude (2.54 × 10^{-5} s^{-1}).

g gravitational acceleration (9.81 m s^{-2}).

h_m^+ minimum mixed layer depth (10 m).

h_k^+ kth layer thickness at which entrainment starts.

h_k^- kth layer thickness at which detrainment starts.

H_o constant reference layer thickness (100 m).

H_k kth layer thickness at rest.

K_H coefficient of horizontal temperature diffusivity (0 $m^2 s^{-1}$).

L_v the latent heat of vaporization.

m_i TKE constants ($m_1 = 6.25$, $m_3 = 7.5$, $m_5 = 1.8$, $m_6 = 0.1$).

n_c TKE constant ($n_c = 1$).

P_a surface air pressure (1013 mbar).

q_l polynomial coefficients for q_{sat} as given by Lowe [1977].

q_{sat} saturated mixing ratio at sea surface.

$\widehat{Q}_{NET}(x,y)$ mean surface heat flux climatology.

R_{gas} the molecular gas constant.

T_b temperature just below the mixed layer (°C).

T_d dewpoint temperature (°C).

$\Delta\rho_k^+$ minimum density contrast for ($\rho_{k+1} - \rho_k$).

ΔT_b temperature shear (°C).

ΔT_b^+ minimum temperature shear (0.2°C).

$\alpha(T)$ coefficient of thermal expansion of sea water ($°C^{-1}$).

ΔT_m temperature change across the mixed layer (°C).

Ω rotation rate of Earth (7.292 × 10^{-5} s^{-1}).

ϕ longitude (degrees).
$\widehat{\rho}_k$ model density climatology for layer k (kg m^{-3}).
ρ_o reference density in the ocean (1000 kg m^{-3}).
σ_ω^{-1} e-folding time for MLD relaxation (1 day).
σ_ρ^{-1} density climatology relaxation e-folding time for $h_k = H_o$.
τ_a surface wind stress.
$\widehat{\omega}_e(x,y)$ mean climatological evaporation rate.
$\widehat{\omega}_k$ kth interface reference vertical mixing velocity.
$\Omega_k(x, y)$ kth interface global mixing correction scale factor.

References

Anderson, S. P., R. A. Weller, and R. B. Lukas, Surface buoyancy forcing and the mixed layer of the western Pacific warm pool: Observations and 1D model results, *J. Clim.*, 9, 3056–3085, 1996.

Arnone, R. A., G. Terrie, L. Estep, and R. A. Oriol, Ocean Optical Database, *NOARL Tech. Note 254*, 36 pp., Naval Res. Lab., Stennis Space Center, Miss., 1992.

Austin, R. W., and T. J. Petzold, Spectral dependence of the diffuse attenuation coefficient of light in ocean waters, *Opt. Eng*, 25, 471–479, 1986.

Baturin, N. G., and P. P. Niiler, Effects of instability waves in the mixed layer of the equatorial Pacific, *J. Geophys Res*, 102, 27,771–27,793, 1997.

Bishop, J. K. B., and W. B. Rossow, Spatial and temporal variability of global surface solar irradiance, *J. Geophys. Res*, 96, 16,839–16,858, 1991

Brock, J. C., C. R McClain, M. E Luther, and W. W. Hay, The phytoplankton bloom in the northwestern Arabian Sea during the southwest monsoon of 1979, *J. Geophys. Res.*, 96, 20,623–20,642, 1991.

Carton, J. A., and Z. Zhou, Annual cycle of sea surface temperature in the tropical Atlantic Ocean, *J Geophys. Res.*, 102, 27,813–27,824, 1997.

Dadou, I., V. Garçon, V. Anderson, G. R. Flierl, and C. S. Davis, Impact of the north equatorial current meandering on a pelagic ecosystem: A modeling approach, *J. Mar. Res.*, 54, 311–342, 1996.

Daley, R., *Atmospheric Data Analysis*, 457 pp., Cambridge Univ. Press, New York, 1991.

Darzi, M., SeaWiFS science algorithm flow chart, *GSFC/CR-1998-206848*, 30 pp., NASA Goddard Space Flight Center, Greenbelt, Md., 1998.

Da Silva, A. M., C. C. Young, and S. Levitus, *Atlas of Surface Marine Data 1994*, vol. 1, *Algorithms and Procedures, NOAA Atlas NESDIS 6*, 83 pp., Natl. Oceanic and Atmos. Admin., Silver Spring, Md., 1994.

European Centre for Medium-Range Weather Forecasts (ECMWF), The description of the ECMWF/WCRP Level III, a global atmospheric data archive European Centre for Medium Range Weather Forecasts technical attachment, Reading, England, 1993.

European Centre for Medium-Range Weather Forecasts (ECMWF), Aspects of the re-analysed climate, *ECMWF Re-Analysis Proj. Rep. Ser.* 2, 89 pp., Reading, England, 1997.

Firestone, E. R., and S. B. Hooker, SeaWiFS prelaunch technical report series final cumulative index, *NASA Tech. Memo., 1998-104566, 43*, 69 pp., 1998.

Flierl, G. R, and C. S. Davis, Biological effects of Gulf Stream meandering, *J. Mar. Res*, 51, 529–560, 1993.

Fu, G., K. S. Baith, and C. R. McClain, SeaDAS: The SeaWiFS Data Analysis System, paper presented at the 4th Pacific Ocean Remote Sensing Conference, NASA Goddard Space Flight Center, Qingdao, China, 1998.

Gallacher, P. C., and P. A. Rochford, Numerical simulations of the Arabian Sea using tracers as proxies for phytoplankton biomass, *J Geophys. Res.*, 100, 18,565–18,579, 1995.

Gallimore, R. G., and D. D. Houghton, Approximation of ocean heat storage by ocean-atmosphere energy exchange: Implications for seasonal cycle mixed layer ocean formulations, *J. Phys. Oceanogr.*, 17, 1214–1231, 1987.

Gordon, H. R., and D. K. Clark, Atmospheric effects in the remote sensing of phytoplankton pigments, *Boundary Layer Meteorol.*, 18, 300–314, 1980.

Hellerman, S., and M. Rosenstein, Normal monthly wind stress over the world ocean with error estimates, *J. Phys. Oceanogr.*, 13, 1093–1104, 1983.

Hurlburt, H. E., and E. J. Metzger, Bifurcation of the Kuroshio Extension at the Shatsky Rise, *J. Geophys. Res.*, 103, 7549–7566, 1998.

Hurlburt, H. E., A. J. Wallcraft, W. J. Schmitz, P. J. Hogan, and E. J. Metzger, Dynamics of the Kuroshio/Oyashio current system using eddy-resolving models of the North Pacific Ocean, *J. Geophys. Res.*, 101, 941–976, 1996.

Jerlov, N. G., *Marine Optics, Elsevier Oceanogr. Ser.*, vol. 14, Elsevier Sci., New York, 1976.

Kantha, H. K., and C. A. Clayson, An improved mixed layer model for geophysical applications, *J. Geophys. Res.*, 99, 25,235–25,266, 1994.

Kara, A. B., P. A. Rochford, and H. E. Hurlburt, Efficient and accurate bulk parameterizations of air-sea fluxes for use in general circulation models, *J Atmos. Ocean. Technol.*, 17, 1421–1438, 2000a.

Kara, A. B., P. A. Rochford, and H. E. Hurlburt, An optimal definition for ocean mixed layer depth, *J. Geophys. Res.*, 105, 16,803–16,821, 2000b.

Keen, T. R., J. C. Kindle, and D. K. Young, The interaction of southwest monsoon upwelling, advection and primary production in the northwest Arabian Sea, *J. Mar. Syst.*, 13, 61–82, 1997.

Kraus, E. B., and J. S. Turner, A one-dimensional model of the seasonal thermocline, II, The general theory and its consequences, *Tellus*, 19, 98–106, 1967.

Large, W. G., J. C. McWilliams, and S. C. Doney, Oceanic vertical mixing: A review and a model with a nonlocal boundary layer parameterization, *Rev. Geophys.*, 32, 363–403, 1994.

Levitus, S., and T. P. Boyer, *World Ocean Atlas 1994*, vol. 4, *Temperature, NOAA Atlas NESDIS 4*, 117 pp., Natl. Oceanic and Atmos. Admin., Silver Spring, Md., 1994.

Levitus, S., R. Burgett, and T. P. Boyer, *World Ocean Atlas 1994*, vol. 3, *Salinity, NOAA Atlas NESDIS 3*, 99 pp., Natl. Oceanic and Atmos. Admin., Silver Spring, Md., 1994.

Lewis, M. R., M. E. Carr, G. Feldman, C. R. McClain, and W. Esaias, Influence of penetrating radiation on the heat budget of the equatorial Pacific Ocean, *Nature*, 347, 543–545, 1990.

Lorenc, A. C., A global three-dimensional multivariate statistical interpolation scheme, *Mon Weather Rev.*, 701–721, 1981.

Lowe, P. R., An approximating polynomial for the computation of saturation vapor pressure, *J. Appl Meteorol.*, 16, 100–103, 1977

Martin, P., Simulation of the mixed layer at OWS November and Papa with several models, *J. Geophys. Res*, 90, 903–916, 1985.

McCreary, J. P., K. E. Kohler, R. R Hood, and D. B. Olsen, A four-component ecosystem model of biological activity in the Arabian Sea, *Prog. Oceanogr.*, 37, 193–240, 1996.

McClain, C. R., M. L. Cleave, G. C. Feldman, W. W. Gregg, S. B. Hooker, and N. Kuring, Science quality SeaWiFS data for global biosphere research, *Sea Technol.*, 39, 10–16, 1998.

McClain, C. R., E. J. Ainsworth, R. A. Barnes, R. E. Eplee Jr., F. S. Patt, W. D. Robinson, M. Wang, and S. W. Bailey, SeaWiFS postlaunch calibration and validation analyses, part 1, *NASA Tech. Memo., 2000-206892*, vol. 9, 82 pp., 2000a.

McClain, C. R., et al., SeaWiFS postlaunch calibration and validation analyses, part 2, *NASA Tech. Memo., 2000-206892*, vol. 10, 57 pp., 2000b.

Meehl, G. A., A calculation of ocean heat storage and effective ocean surface layer depths for the Northern Hemisphere, *J. Phys Oceanogr.*, 14, 1747–1761, 1984.

Metzger, E. J., and H. E. Hurlburt, Coupled dynamics of the South China Sea, the Sulu Sea, and the Pacific Ocean, *J. Geophys. Res.*, 101, 12,331–12,352, 1996.

Metzger, E. J., and H. E. Hurlburt, The nondeterministic nature of Kuroshio Penetration and eddy shedding in the South China Sea, *J. Phys. Oceanogr.*, 31, 1712–1732, 2001.

Metzger, E. J., H. E. Hurlburt, J. C. Kindle, Z. Sirkes, and J. M. Pringle, Hindcasting of wind-driven anomalies using a reduced-gravity global ocean model, *Mar. Technol. Soc. J.*, 26, 23–32, 1992.

Mobley, C. D., *Light and Water*, 592 pp., Academic, San Diego, Calif., 1994.

Morel, A., Optical modeling of the upper ocean in relation to its biogenous matter content (case I waters), *J. Geophys. Res.*, 93, 10,749–10,768, 1988.

Morel, A., and D. Antoine, Heating rate within the upper ocean in relation to its bio-optical state, *J. Phys. Oceanogr.*, 24, 1652–1665, 1994.

Murphy, A. H., Skill scores based on the mean square error and their

relationships to the correlation coefficient, *Mon. Weather Rev.*, *116*, 2417–2424, 1995.

Murtugudde, R., M. Cane, and V. Prasad, A reduced-gravity, primitive equation, isopycnal ocean GCM: Formulation and simulations, *Mon. Weather Rev.*, *123*, 2864–2887, 1995.

Niiler, P. P., and E. B. Kraus, One-dimensional models of the upper ocean, in *Modeling and Prediction of the Upper Layers of the Ocean*, pp. 143–172, Pergamon, New York, 1977.

O'Reilly, J. E., et al., SeaWiFS postlaunch calibration and validation analyses, part 3, *NASA Tech Memo. 2000-206892*, *11*, 49 pp., 2000.

Paulson, C. A., and J. J. Simpson, Irradiance measurements in the upper ocean, *J. Phys. Oceanogr.*, *7*, 952–956, 1977.

Platt, T., S. Sathyrendranath, C. M. Caverhill, and M. R. Lewis, Ocean primary production and available light: Further algorithms for remote sensing, *Deep Sea Res.*, *35*, 855–879, 1988.

Rochford, P. A., J. C. Kindle, P. C. Gallacher, and R. A. Weller, Sensitivity of the Arabian Sea mixed layer to 1994-1995 operational wind products, *J. Geophys. Res.*, *105*, 14,141–14,162, 2000.

Schopf, P. S., and A. Loughe, A reduced-gravity isopycnal ocean model: Hindcasts of El Niño, *Mon. Weather Rev.*, *123*, 2839–2863, 1995.

Shriver, J. F., and H. E. Hurlburt, The contribution of the global thermohaline circulation to the Pacific to Indian Ocean throughflow via Indonensia, *J. Geophys. Res.*, *102*, 5491–5511, 1997.

Sterl, A., and A. Kattenberg, Embedding a mixed layer model into an ocean general circulation mode of the Atlantic: The importance of surface mixing for heat flux and temperature, *J. Geophys. Res.*, *99*, 14,139–14,157, 1994.

Stevenson, J. W., and P. P. Niiler, Upper ocean heat budget during the Hawaii-to-Tahiti shuttle experiment, *J. Phys. Oceanogr.*, *13*, 1894–1907, 1983.

White, W. B., D. R. Cayan, and J. Lean, Global upper ocean heat storage to radiative forcing from changing solar irradiance and increasing greenhouse gas/aerosol concentrations, *J. Geophys. Res.*, *103*, 21,355–21,366, 1998.

Woods, J. D., W. Barkman, and A. Horch, Solar heating of the oceans, diurnal, seasonal and meridional variation, *Q. J. R. Meteorol. Soc*, *110*, 633–656, 1984.

Yuen, C. W., J. Y. Cherniawsky, C. A. Lin, and L. A. Mysak, An upper ocean general circulation model for climate studies: Global simulation with seasonal cycle, *Clim. Dyn*, *7*, 1–18, 1992.

Zaneveld, J. R., and R. W. Spinrad, An arctangent model of irradiance in the sea, *J. Geophys. Res.*, *85*, 4919–4922, 1980.

Zaneveld, J. R., J. C. Kitchen, and H. Pak, The influence of optical water type on the heating rate of a constant depth mixed layer, *J. Geophys Res.*, *96*, 6426–6428, 1981.

Zaneveld, J. R., J. C. Kitchen, and J. L. Müeller, Vertical structure of productivity and its vertical integration as derived from remotely sensed observations, *Limnol. Oceanogr*, *38*, 1384–1393, 1993.

R. A. Arnone, P. A. Rochford, and A. J. Wallcraft, Oceanography Division, Naval Research Laboratory, Stennis Space Center, Mississippi, MS 39529, USA. (arnone@nrlssc.navy.mil; rochford@nrlssc.navy.mil; wallcraft@nrlssc.navy.mil)

A. B. Kara, Center for Ocean-Atmospheric Prediction Studies, Florida State University, Tallahassee, FL 32306, USA.